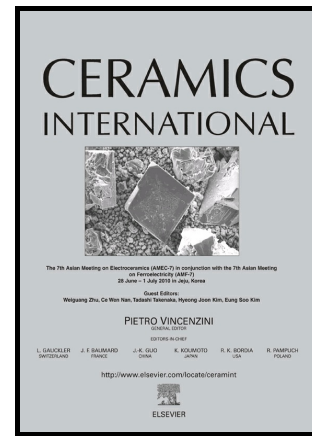


Author's Accepted Manuscript

Synthesis of a cubic Ti(BCN) advanced ceramic by a solid-gas mechanochemical reaction

E. Chicardi, C. García-Garrido, A.M. Beltrán, M.J. Sayagués, F.J. Gotor



PII: S0272-8842(18)33166-3
DOI: <https://doi.org/10.1016/j.ceramint.2018.11.060>
Reference: CERI20034

To appear in: *Ceramics International*

Received date: 27 August 2018
Revised date: 11 October 2018
Accepted date: 9 November 2018

Cite this article as: E. Chicardi, C. García-Garrido, A.M. Beltrán, M.J. Sayagués and F.J. Gotor, Synthesis of a cubic Ti(BCN) advanced ceramic by a solid-gas mechanochemical reaction, *Ceramics International*, <https://doi.org/10.1016/j.ceramint.2018.11.060>

This is a PDF file of an unedited manuscript that has been accepted for publication. As a service to our customers we are providing this early version of the manuscript. The manuscript will undergo copyediting, typesetting, and review of the resulting galley proof before it is published in its final citable form. Please note that during the production process errors may be discovered which could affect the content, and all legal disclaimers that apply to the journal pertain.

Synthesis of a cubic Ti(BCN) advanced ceramic by a solid-gas mechanochemical reaction

E. Chicardi^{1*}, C. García-Garrido², A. M. Beltrán¹, M. J. Sayagués², F. J. Gotor²

¹Departamento de Ingeniería y Ciencia de los Materiales y del Transporte, Escuela Politécnica de Sevilla, Universidad de Sevilla (ESI-US). C/ Virgen de África 7, 41011 Sevilla, Spain.

²Instituto de Ciencia de Materiales de Sevilla (CSIC-US), Américo Vespucio 49, 41092 Sevilla, Spain.

*Corresponding author. echicardi@us.es

Abstract.

In this work, a titanium boron carbonitride advanced ceramic was successfully synthesised by a solid-gas mechanochemical reaction in a planetary ball mill from a mixture of elemental Ti, B, and C under nitrogen atmosphere. This material, with a general formula of Ti(BCN), exhibits a face-centred cubic structure (NaCl type) that is analogous to Ti(CN). This phase was gradually formed with sufficient milling time as a result of diffusional processes, which were permitted by the reduction of the energy in the system caused by the decrease in the spinning rate of the planetary ball mill. In contrast, under more energetic milling conditions, a mechanically induced self-sustaining reaction (MSR) took place, leading to the formation of a TiB₂-Ti(CN) ceramic composite. The microstructural characterisation revealed that Ti(BCN) was composed of ceramic particles constituted of misoriented nanocrystalline domains. B, C and N were optimally distributed in the Ti(BCN) phase. The TiB₂-Ti(CN) ceramic composite was composed of micrometric and nanometric particles homogeneously distributed. Additionally, the nitrogen content obtained for Ti(BCN) was higher than for the Ti(CN) phase in the composite material.

Keywords: titanium boron carbonitride; advanced ceramic; titanium carbonitride; titanium diboride; solid-gas reaction; mechanochemistry.

1. INTRODUCTION.

Titanium carbonitride, Ti(CN), and titanium diboride, TiB₂, are advanced structural ceramics with wide technological applications due to their appealing properties. Ti(CN) is mainly used for ceramic coatings and as the main ceramic component in cermets utilised in cutting tools [1-4] owing to its high refractoriness, heat conductivity, hardness, wear and corrosion resistance, edge strength, edge sharpness and low density [1, 5-8]. Ti(CN)-based cermets are also potential candidates for other interesting structural applications, such as in components of aircraft gas turbines, automobile engines, bearings, machines for mineral operations, and more [9]. TiB₂ is an ultra-high temperature ceramic (UHTC) with a high specific strength, durability, melting point, thermal conductivity, hardness and wear resistance [10-12] that is applied as a coating for cutting tools, wear-resistant parts, high-temperature structural materials, lightweight impact-resistant armour materials, electrode materials, and more [13]. TiB₂-Ti(CN) composites have been proposed for several applications [14-17] because the mixing of these two materials leads to a synergistic effect that creates superior mechanical properties when compared to the individual ceramic components.

New advances have been carried out to further improve some of the properties of these ceramics, of which the hardness and the wear resistance have been a particular focus. In this context, a new and interesting material based on the Ti-B-C-N system was successfully developed with chemical formula Ti(BCN) [18, 19]. This compound

presents with a face-centred cubic structure (fcc, NaCl-type structure) that is analogous to the Ti(CN) ceramic phase, [20] where the boron is placed in the same crystallographic positions as C and N. It has been successfully synthesised and deposited as a protective coating for high-speed steels (HSS), hard metals (WC-Co) and niobium-, molybdenum- and aluminium-based alloy substrates for cutting tools. When compared to ceramic coatings made of TiB₂, TiN and Ti(CN), this composite ceramic is superior in its ability to increase the hardness (to greater than 4000 Vickers Hardness), improve both the flank wear resistance [20, 21] and the corrosion resistance, and diminish the friction coefficient [22]. These coatings have been developed by magnetron sputtering (MS), ion beam assisted deposition (IBA) and physical and chemical vapour deposition (PVD and CVD, respectively), among other methods.

However, there are no synthetic methods that have been able to produce ultra-hard Ti(BCN) at a bulk scale. Therefore, in this work, we propose a bulk synthesis of both the Ti(CN)-TiB₂ ceramic composite and the Ti(BCN) advanced ceramic by solid-gas mechanochemical procedures. Notably, both materials were obtained by milling mixtures of elemental Ti, B and C in a nitrogen atmosphere using a planetary mill. The key parameter for selecting the intended material was the spinning rate of the planetary mill, which directly determines the energy transferred to the powder reactant mixture, since it controls both the intensity and the frequency of the ball collisions. Specifically, the intensity of the milling determined whether or not a mechanically induced self-sustaining reaction (MSR) occurred, where an MSR forms the TiB₂-Ti(CN) composite material while an absence of an MSR forms cubic-phase Ti(BCN). The proposed mechanochemical synthesis offers a direct and cost-effective route to obtain large quantities of Ti(BCN) without the requirement of added heat while using a solvent-free chemical process [23]. Similar solid-gas mechanochemical reactions have been

successfully applied to induce chemical reactions in a wide variety of high-exothermic powder mixtures [23, 24]. This has led to the direct synthesis of Ti(CN) [25], Ti(CN)-based cermets [25] or complex solid solutions of titanium-tantalum-niobium carbonitrides.

2. EXPERIMENTAL PROCEDURE.

An elemental powder mixture of titanium (99% purity, 325 mesh, Alfa Aesar), graphite (99% purity, 325 mesh, Alfa Aesar) and boron (98% purity, 325 mesh, Alfa Aesar) with a Ti/B/C atomic ratio equivalent to a nominal composition of 50 wt.% $\text{TiC}_{0.5}\text{N}_{0.5}$ and 50 wt.% TiB_2 was used along with nitrogen (H_2O and $\text{O}_2 < 63$ ppm, Air Liquide) as reactive gas. Five grams of the Ti/C/B mixture was added into a 45 ml tempered steel vial (67HRC) together with 7 stainless-steel balls (AISI 420C, 15 mm of diameter and 13.2 g) to create a powder-to-ball ratio (PBR) of 19.2. The contents of the vial were milled under 5 bar of N_2 in a modified *Pulverisette 7* (Fritsch, Germany) planetary ball mill. Two different spinning rates were used—600 rpm (600TiBCN) and 300 rpm (300TiBCN)—and the milling process was carried out at cyclic intervals of 5 h ON and 30 min OFF in order to reduce the temperature inside the vial. The introduction of the N_2 gas pressure was made possible by modifying the *Pulverisette 7* ball mill by connecting the vial to the gas cylinder via a rotating union (model 1005-020-038, Deublin) and a flexible polyamide tube. The N_2 gas pressure was monitored continuously with a pressure transducer (AKS, Danfoss) connected to a paperless recorder (Ecograph T RSG35, Endress + Hauser). The planetary mill was able to detect MSR processes, since the temperature increase caused by the exothermic reaction produces an instantaneous increase in the total pressure, and a spike was observed in the recorded time–pressure data.

X-ray diffraction patterns (XRD) were obtained by a PANalytical X'Pert Pro instrument equipped with a θ/θ goniometer, a Cu K α radiation source (40 kV, 40 mA), a secondary K β filter and an X'Celerator detector. They were collected with a 2θ range between 20° and 150° with 0.02° steps and a counting time of $275 \text{ s}\cdot\text{step}^{-1}$. The space group symmetry (SGS), lattice parameters, crystalline domain size (D) and microstrain (ϵ) of the phases were determined from the set of peaks in the XRD diagrams using Dicvol software and the Williamson-Hall equation. Additionally, the Crystallography Open Database (COD) was used for comparison and structural elucidation. Lanthanum hexaboride (LaB $_6$, Standard Reference Material 660b, NIST) was used to calibrate the positions of the diffraction peaks.

Scanning-transmission electron microscopy (STEM) experiments were performed using an FEI Talos F200S microscope operating at an accelerating voltage of 200 kV and equipped with a Super-X energy dispersive X-ray spectrometry (EDS) system that includes two silicon drift detectors. The elemental mapping experiments were performed by combining high-angle annular dark field imaging (HAADF) and EDX acquisitions in STEM mode. For the TEM experiments, samples have been directly deposited on a holey carbon film on a copper grid.

The amounts of C and N in the samples were determined by elemental analysis using a LECO elemental analyser (mod. CNHS-932).

The X-ray photoelectron spectroscopy (XPS) measurements were carried out in the UHV chamber equipped with a multichannel hemispherical analyser VG ESCALAB 210. The Al K α X-Ray source (13kV and 15mA) was used as X-Ray excitation source.

3. RESULTS AND DISCUSSION.

When the milling process was carried out at 600 rpm (sample hereon denoted by 600TiBCN), an important pressure increase was detected in the time–pressure record after 44 min of milling, which was evidence for the occurrence of an MSR process [23, 26, 27]. The milling process was extended 30 min after the observed MSR process to homogenise the as-synthesised powders. However, when the powder mixture was milled at 300 rpm (sample hereon denoted by 300TiBCN), no exothermic reaction was detected, even after milling for 60 h. When the 300TiBCN sample was subsequently remilled at 600 rpm for 1 h, an MSR process was not observed, suggesting that the chemical nature of the Ti/B/C mixture was modified during milling at 300 rpm.

To study the phases developed in both 600TiBCN and 300TiBCN powder samples during milling, XRD patterns were collected and are shown in Fig. 1a. For the 600TiBCN sample, both of the expected phases after the MSR reaction were observed [26, 27], i.e., titanium carbonitride, Ti(CN), with fcc structure (*Fm-3m*) and hexagonal TiB₂ (*P6/mmm*). The position of the XRD peaks for TiB₂ clearly matches that of the TiB₂ reference no. 2002799 of the Crystallography Open Database (COD) (marked as a continuous line in Fig. 1b). This aspect is not surprising, as TiB₂ is considered as a stoichiometric compound. The XRD peaks for the Ti(CN) (reference no. phase are located between the corresponding peaks of TiC and TiN, according to the references no. 1539505 and 1101045 of the COD (dotted and dashed lines in Fig. 1b, respectively) and confirming the formation of a carbonitride phase. The presence of both C and N will be corroborated later by elemental analysis and HAADF-EDS mappings.

For the 300TiBCN sample where the MSR reaction was not detected, the XRD pattern (Fig 1a) surprisingly showed only the presence of an *Fm-3m* cubic phase. In addition, slight peaks corresponding to unreacted Ti (hcp, *P63/mmc*) and Fe (bcc, *Im3m*) were detected, which can be attributed to contamination from the milling media.

The apparent absence of any other crystalline boron compound suggests that boron was part on this cubic phase, most likely dissolved into the fcc structure. As seen in Fig 1b, the XRD pattern of this fcc phase is displaced to higher 2θ values in comparison with the fcc phase in 600TiBCN. This fact is evidence for the introduction of B into the fcc Ti(CN) structure, forming a fcc Ti(BCN) phase. Note that the observed displacement may also be explained by the presence of a greater amount of N in the structure.

From the XRD peaks in 600TiBCN and 300TiBCN samples, the lattice parameters were determined for the TiB₂-Ti(CN) and Ti(BCN) phases, respectively (Table 1). For comparison purposes, the lattice parameters of TiB₂, TiC and TiN from the COD reference patterns are also given. We observed that the lattice parameters for TiB₂ matched perfectly with the COD reference, while the lattice parameters for the supposed Ti(CN) and Ti(BCN) phases were both between the values for TiC and TiN references. The crystalline domain size (D) and the microstrain (ϵ) for each phase in the 600TiBCN and 300TiBCN samples were also determined (Table 1). For 600TiBCN, D values of 63 and 85 nm were calculated for TiB₂ and Ti(CN), respectively. For 300TiBCN, the D value was 6 nm, which is one order of magnitude lower. The smaller domains are most likely caused by the long milling time used for 300TiBCN. The same trend was observed in the microstrain content (Table 1); the longer milling time induced a higher level of defects in the material.

Elemental analysis was carried out to quantify the amounts of C and N and to estimate the C/N stoichiometry in the Ti(CN) and Ti(BCN) phases formed in the 600TiBCN and 300TiBCN samples, respectively. The results (Table 1) showed a much higher N content and lower C/N atomic ratio in Ti(BCN) than in Ti(CN). Taking into account these values for the N content and the starting atomic ratio in the powder mixture (also the B and the extra Ti amount, initially added to form the titanium

diboride) the estimated stoichiometry for Ti(CN) and Ti(BCN) were $\text{TiC}_{0.50}\text{N}_{0.33}$ and $\text{TiBC}_{0.25}\text{N}_{0.79}$, respectively. This higher N amount and the presence of B contributed to the previously observed 2θ displacement to higher angles in the XRD pattern (Fig. 1b) of Ti(BCN) in comparison with Ti(CN). Therefore, a larger amount of N was introduced into the fcc structure when the milling process was performed at a lower intensity (i.e., at a lower speed), such that N was incorporated continuously with milling time through a diffusion process and not instantaneously through a self-sustaining reaction. When compared to TiC, TiN exhibits a higher hardness, while TiB_2 exhibits improved wear resistance [28, 29]. These results suggest that the higher N amount and the presence of B in Ti(BCN) could produce an important increase in these properties.

To study the morphology of the particles and corroborate the composition and the structure of the phases present in the 600TiBCN and 300TiBCN samples, TEM, HRTEM and HAADF-EDS analyses were carried out. The TEM images collected in bright field mode (Fig. 2) showed larger particles in 600TiBCN than in 300TiBCN, which is clearly an effect of the different milling conditions. In 600TiBCN, the highly exothermic MSR process produced after 44 min caused an increase in temperature and facilitated the particle growth. The formation of a partial liquid phase during MSR can favour the growth of larger particles [25]. In contrast, 300TiBCN was milled for 60 h with no MSR, avoiding the increase of the temperature and facilitating the fracturing of particles. Another difference was that 600TiBCN displayed faceted morphologies, while rounded morphologies were observed for 300TiBCN. This difference was also caused by the different milling conditions. The particles observed in 600TiBCN are single crystals with D values approximately 100 nm. In contrast, the particles observed in 300TiBCN showed a polycrystalline nature, with D values lower than 10 nm that corroborated the D values determined by XRD (see Table 1).

The HAADF-EDS mappings allowed for the determination of the qualitative composition of the phases. The EDS mapping for 600TiBCN given in Fig. 3 provides an example of an elongated TiB_2 particle surrounded by the $\text{Ti}(\text{CN})$ phase. Another interesting aspect is the growth of the cubic fcc- $\text{Ti}(\text{CN})$ on the surface of the hcp- TiB_2 particles. The good distribution of both ceramic phases (at a nanometre scale) was possible thanks to the ability of the MSR process to synthesise both phases simultaneously. On the other hand, the HAADF-EDS mapping for 300TiBCN (Fig. 4) shows a homogeneous distribution of Ti, B and N in the particles, corroborating the formation of a single $\text{Ti}(\text{BCN})$ phase. Note that the C element was not shown in either EDS mapping due to high interference from the carbon film of the TEM copper grid.

HRTEM images and the corresponding diffraction patterns obtained from the Fast Fourier Transforms (FFT) are shown in Figs. 5 and 6 for 600TiBCN and 300TiBCN, respectively. Note that FFT are equivalent to electron diffraction patterns (EDP) when the HRTEM micrographs are recorded under Fraunhofer Diffraction conditions. FFT digital diffractograms reveal information about the crystalline structure. Distances and angles between spots have been utilised to index the diffractograms. In the data obtained for 600TiBCN (Fig. 5), two different phases were observed that correspond to TiB_2 and $\text{Ti}(\text{CN})$. The interplanar distances matched well with the distances found by XRD (for comparison purposes, all distances determined by XRD and FFT are displayed in Table 2). Specifically, the (001) crystallographic plane for TiB_2 and the (111), (200) and (220) for $\text{Ti}(\text{CN})$ were all indexed.

Fig. 6 displays an HRTEM image of the 300TiBCN sample along with the corresponding FFT diffraction pattern. The results agree with the interplanar distances obtained from XRD (Table 2). In addition, no distances or angles for the TiB_2 phase were found in 300TiBCN, corroborating the absence of this phase and, therefore, the

inclusion of boron in the fcc-TiBCN structure. For this phase, only the (111) and (200) crystallographic planes could be detected. In addition, small amorphous areas were also observed between nanocrystalline domains with different orientations.

Finally, the XPS study for the B1s region was carried out for the 300TiBCN and 600TiBCN specimens to corroborate the chemical interactions of boron (Fig. 7). For the 600TiBCN it was observable the peak corresponding to the Ti-B bond in the TiB_2 compound (187.5 eV). However, for the 300TiBCN, this peak undergoes a chemical shift from 187.5 eV to 188.6 eV, indicating possible interactions of C and N in the Ti-B bond and also the variation of the coordination environment of boron from dodecahedral coordination (TiB_2) to octahedral coordination ($Ti(BCN)$). Thus, these aspects corroborate the formation of the $Ti(BCN)$ compound abovementioned. By other hand, it is important to comment the presence of B_2O_3 , attributed to a partially oxidation of the surface of the particles. The superficial nature of the XPS made possible the detection of this oxidized compound.

CONCLUSIONS.

In this study, a nanostructured titanium boron-carbonitride ceramic material, $Ti(BCN)$, that presents with a face-centred cubic structure was successfully synthesised via a mechanochemical process. This synthesis was made possible by the suppression of the MSR exothermic reaction that is typical in the Ti-B-C-N system, which was achieved by reducing the spinning rate of the mill, sufficiently reducing the energy in the system. Thus, $Ti(BCN)$ was synthesised by a gradual diffusion of B, C and N into the Ti matrix. This mechanochemical method allows for the fabrication of this advanced ceramic material in a large-scale, inexpensive and reproducible manner.

Moreover, a $\text{TiB}_2\text{-Ti(CN)}$ ceramic composite was also successfully synthesised by utilising an MSR process with the same elemental powder mixture used for the Ti(BCN) synthesis. Because both phases of the composite are formed simultaneously, they were mixed with a uniform distribution at nanometre scales.

Acknowledgements.

This work was supported by the Spanish government under grant No. MAT2014-52407-R, which was financed in part by the European Regional Development Fund. The authors thank the University of Seville for the use of its general research service (CITIUS) under the grant VIPPIT-2018-I.5. They also thank the Laboratory for Nanoscopies and Spectroscopies (LANE) at the ICMS-CSIC for providing access to the TEM facilities.

Fig 1. a) X-ray diffraction (XRD) patterns for the 600TiBCN and 300TiBCN samples. (■) TiB₂; (●) Ti(CN); (◆) Ti(BCN); (♣) Ti hcp; (★) Fe. b) Magnification of the XRD patterns in the 33°–43° 2θ range showing the displacements of the (111) and (200) Ti(CN) peaks. Continuous, dotted and dashed lines designate the positions for the corresponding reflections of TiB₂, TiC and TiN, respectively.

Fig 2. Transmission Electron Microscope (TEM) images for the 600TiBCN and 300TiBCN samples.

Fig 3. High-angle annular dark field image (HAADF) and Energy-Dispersive X-ray Spectroscopy (EDS) mapping for 600TiBCN.

Fig 4. High-angle annular dark field image (HAADF) and Energy-Dispersive X-ray Spectroscopy (EDS) mapping for 300TiBCN.

Fig 5. a) High-resolution TEM (HRTEM) image for 600TiBCN showing the presence of both Ti(CN) and TiB₂ phases. b) Fast Fourier Transform (FFT) image obtained from the 600TiBCN HRTEM image. Numbers 1, 2, 3 and 4 (marked also in Figure 5a) correspond to crystallographic planes detected for both the TiB₂ and Ti(CN) phases.

Fig 6. a) High-resolution TEM (HRTEM) image for 300TiBCN showing the presence of Ti(BCN) that is unique to this sample. b) Fast Fourier Transform (FFT) image obtained from the 300TiBCN HRTEM image. Numbers 1, 2 and 3 (marked also in Figure 5a) correspond to crystallographic planes detected for the Ti(BCN) phase. Number 4 correspond to an amorphous zone detected between nanocrystals with different orientations.

Fig 7. XPS spectra for the B1s region of the 300TiBCN and 600TiBCN specimens.

Table 1. Lattice parameters (\AA), crystalline domain size (D), microstrain (e) and C and N compositions for the TiB_2 and $\text{Ti}(\text{CN})$ phases in 600TiBCN and the $\text{Ti}(\text{BCN})$ phase in 600TiBCN. For comparison purposes, the lattice parameters for TiB_2 , TiC and TiN from the COD database are also given.

Sample		
600TiBCN	300TiBCN	
Phases		
TiB_2	$\text{Ti}(\text{CN})$	$\text{Ti}(\text{BCN})$
Lattice parameters (\AA) by XRD and from the COD*		
a=b= 3.029; c= 3.221	a=b=c= 4.301	a=b=c= 4.242
*For comparison purposes:		
TiB_2 (ref.no. 2002799): a=b= 3.029; c= 3.228		
TiC (ref.no. 9012564): a=b=c= 4.328		
TiN (ref.no. 1100037): a=b=c= 4.239		
D (nm)		
63	85	6
e (%)		
0.001	0.003	0.010
Absolute C amount (wt. %)		
-	3.7 ± 1.0	3.6 ± 0.3
Absolute N amount (wt. %)		

-	2.9 ± 0.9	13.7 ± 1.3
C/N atomic ratio		
-	1.5	0.3

Table 2. Interplanar distances (nm) for the TiB_2 and $Ti(CN)$ phases in the 600TiBCN sample and $Ti(BCN)$ phase in the 300TiBCN sample, as determined by XRD and HRTEM-FFT.

Crystallographic planes	Sample					
	600TiBCN			300TiBCN		
	Phases					
	TiB_2		$Ti(CN)$		$Ti(BCN)$	
	XRD	HRTEM-FFT	XRD	HRTEM-FFT	XRD	HRTEM-FFT
(111)	-	-	0.248	0.250	0.245	0.242
(200)	-	-	0.215	0.217	0.212	0.210
(220)	-	-	0.152	0.155	0.150	N.D.
(001)	0.323	0.322	-	-	-	-
(100)	0.262	N.D.	-	-	-	-
(101)	0.203	N.D.	-	-	-	-

REFERENCES.

- [1] S. Zhang, Titanium carbonitride-based cermets: processes and properties, *Materials Science and Engineering A*, 163 (1993) 141-148.
- [2] S. Zhang, Material development of titanium carbonitride-based cermets for machining application, 1998, pp. 521-543.
- [3] H. Zhang, J. Yan, X. Zhang, S. Tang, Properties of titanium carbonitride matrix cermets, *International Journal of Refractory Metals and Hard Materials*, 24 (2006) 236-239.
- [4] G. Levi, W.D. Kaplan, M. Bamberger, Structure refinement of titanium carbonitride (TiCN), *Materials Letters*, 35 (1998) 344-350.
- [5] E. Chicardi, J.M. Cordoba, F.J. Gotor, High temperature oxidation resistance of (Ti,Ta)(C,N)-based cermets, *Corrosion Science*, 102 (2016) 125-136.
- [6] E. Chicardi, J.M. Cordoba, F.J. Gotor, Kinetics of high-temperature oxidation of (Ti,Ta)(C,N)-based cermets, *Corrosion Science*, 102 (2016) 168-177.
- [7] P. Angerer, L.G. Yu, K.A. Khor, G. Korb, I. Zalite, Spark-plasma-sintering (SPS) of nanostructured titanium carbonitride powders, *Journal of the European Ceramic Society*, 25 (2005) 1919-1927.
- [8] W. Lengauer, Transition Metal Carbides, Nitrides, and Carbonitrides, in: R. Riedel (Ed.) *Handbook of Ceramic Hard Materials* 2008.
- [9] E.B. Clark, B. Roebuck, Extending the application areas for titanium carbonitride cermets, *International Journal of Refractory Metals and Hard Materials*, 11 (1992) 23-33.
- [10] R.G. Munro, Material properties of titanium diboride, *Journal of Research of the National Institute of Standards and Technology*, 105 (2000) 709-720.
- [11] I. Sulima, TRIBOLOGICAL PROPERTIES OF STEEL/TiB₂ COMPOSITES PREPARED BY SPARK PLASMA SINTERING, *Arch. Metall. Mater.*, 59 (2014) 1263-1268.
- [12] B.R. Golla, T. Bhandari, A. Mukhopadhyay, B. Basu, Titanium Diboride, in: W.G. Fahrenholtz, E.J. Wuchina, W.E. Lee, Y. Zhou (Eds.) *Ultra-High Temperature Ceramics* 2014.
- [13] B. Basu, G.B. Raju, A.K. Suri, Processing and properties of monolithic TiB₂ based materials, *International Materials Reviews*, 51 (2006) 352-374.
- [14] X.R. Zhao, D.W. Zuo, M.X. Zhang, F. Xu, S.S. Feng, In situ production of ultra-fine Ti(C,N)-TiB₂-Co cermets by reactive hot processing from the Co-Ti-C-BN system, *International Journal of Refractory Metals & Hard Materials*, 55 (2016) 1-10.
- [15] G.J. Zhang, Z.Z. Jin, X.M. Yue, TiB₂-Ti(C,N)-SiC composites prepared by reactive hot pressing, *Journal of Materials Science Letters*, 15 (1996) 26-28.
- [16] E. Shankar, S.B. Prabu, K.A. Padmanabhan, Mechanical properties and microstructures of TiCN/nano-TiB₂/TiN cermets prepared by spark plasma sintering, *Ceramics International*, 44 (2018) 9384-9394.
- [17] S. Shimada, A. Takahashi, H. Kiyono, J. Tsujino, Coatings and microstructures of monolithic TiB₂ films and double layer and composite TiCN/TiB₂ films from alkoxide solutions by thermal plasma CVD, *Thin Solid Films*, 516 (2008) 6616-6621.
- [18] D. Zhong, E. Sutter, J.J. Moore, G.G.W. Mustoe, E.A. Levashov, J. Disam, Mechanical properties of Ti-B-C-N coatings deposited by magnetron sputtering, *Thin Solid Films*, 398-399 (2001) 320-325.
- [19] D.E. Wolfe, J. Singh, Synthesis and characterization of TiBCN coatings deposited by ion beam assisted, co-evaporation electron beam-physical vapor deposition (EB-PVD), *Journal of Materials Science*, 37 (2002) 3777-3787.
- [20] J. Lin, J.J. Moore, B. Mishra, M. Pinkas, W.D. Sproul, The structure and mechanical and tribological properties of TiBCN nanocomposite coatings, *Acta Materialia*, 58 (2010) 1554-1564.
- [21] S. Shimada, M. Takahashi, J. Tsujino, I. Yamazaki, K. Tsuda, Deposition and wear resistance of Ti-B-N-C coatings on WC-Co cutting tools from alkoxide solutions by thermal plasma CVD, *Surface and Coatings Technology*, 201 (2007) 7194-7200.

- [22] Y. Li, P. Zhang, P. Bai, L. Wu, B. Liu, Z. Zhao, Microstructure and properties of Ti/TiBCN coating on 7075 aluminum alloy by laser cladding, *Surface and Coatings Technology*, 334 (2018) 142-149.
- [23] L. Takacs, Self-sustaining reactions induced by ball milling, *Progress in Materials Science*, 47 (2002) 355-414.
- [24] L. Takacs, The historical development of mechanochemistry, *Chemical Society Reviews*, 42 (2013) 7649-7659.
- [25] E. Chicardi, F.J. Gotor, M.D. Alcala, J.M. Cordoba, Effects of additives on the synthesis of TiC_xN_{1-x} by a solid-gas mechanically induced self-sustaining reaction, *Ceramics International*, 44 (2018) 7605-7610.
- [26] E. Chicardi, F.J. Gotor, M.D. Alcala, J.M. Cordoba, Influence of milling parameters on the solid-gas synthesis of TiC_xN_{1-x} by mechanically induced self-sustaining reaction, *Powder Technology*, 319 (2017) 12-18.
- [27] M.A. Aviles, J.M. Cordoba, M.J. Sayagues, F.J. Gotor, Mechanochemical synthesis of $Ti_{1-x}Zr_xB_2$ and $Ti_{1-x}Hf_xB_2$ solid solutions, *Ceramics International*, 37 (2011) 1895-1904.
- [28] D. Martinez-Martinez, C. Lopez-Cartes, A. Fernandez, J.C. Sanchez-Lopez, Comparative performance of nanocomposite coatings of TiC or TiN dispersed in a-C matrixes, *Surf. Coat. Technol.*, 203 (2008) 756-760.
- [29] D. Vallauri, I.C. Atías Adrián, A. Chrysanthou, TiC–TiB₂ composites: A review of phase relationships, processing and properties, *Journal of the European Ceramic Society*, 28 (2008) 1697-1713.

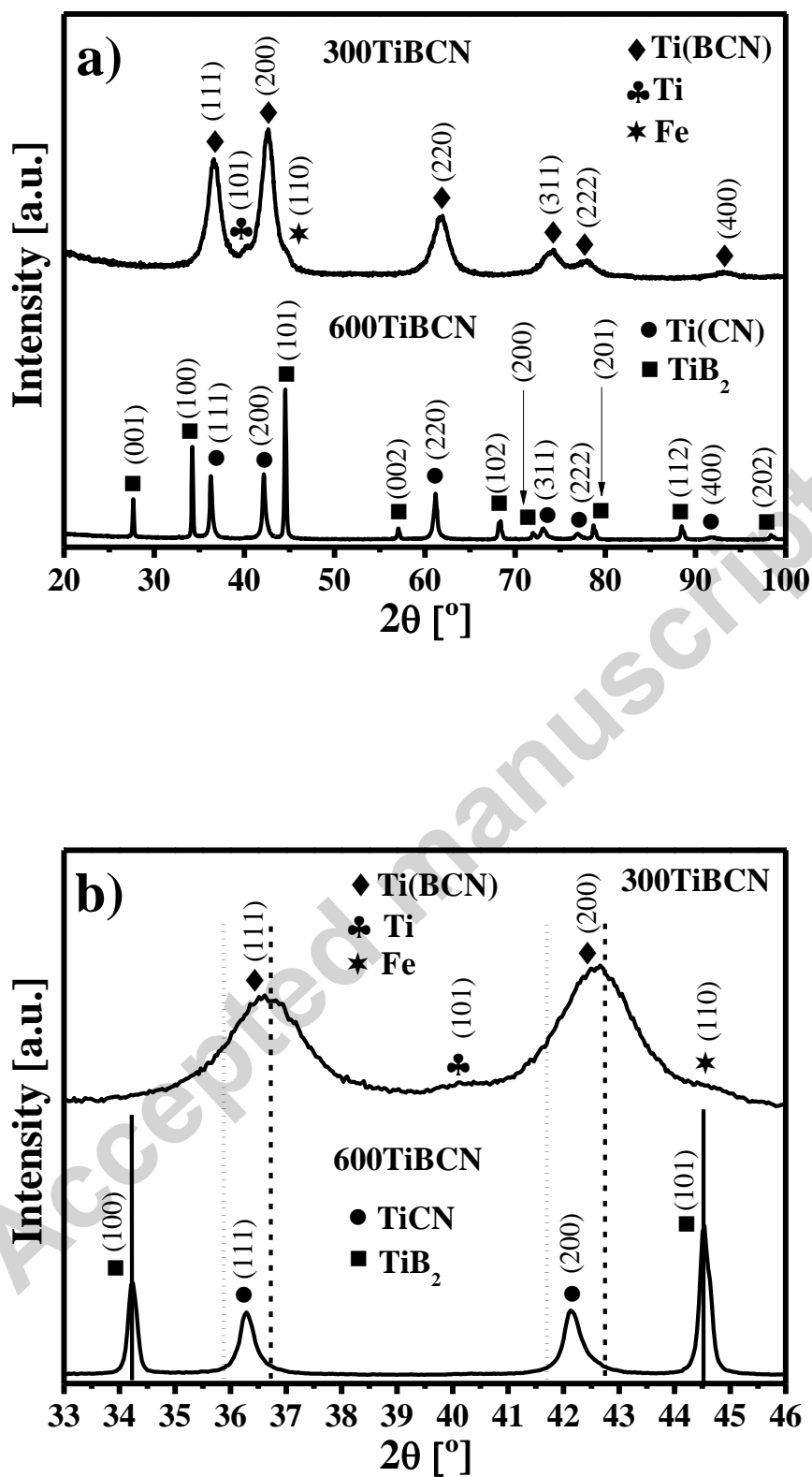


Figure 1
17

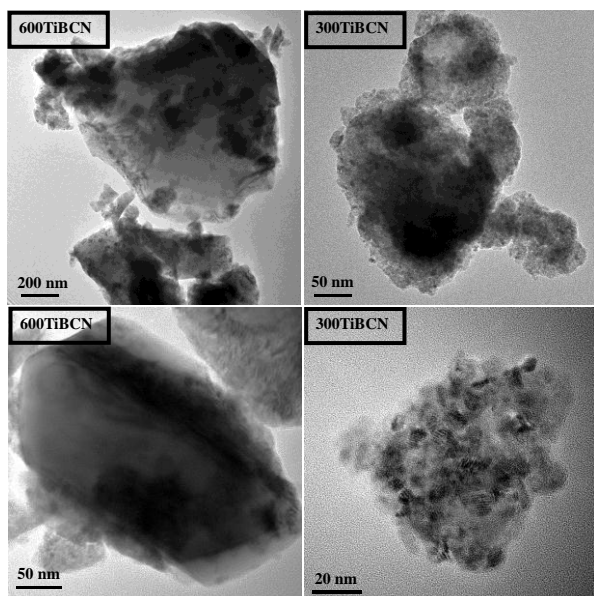


Figure 2

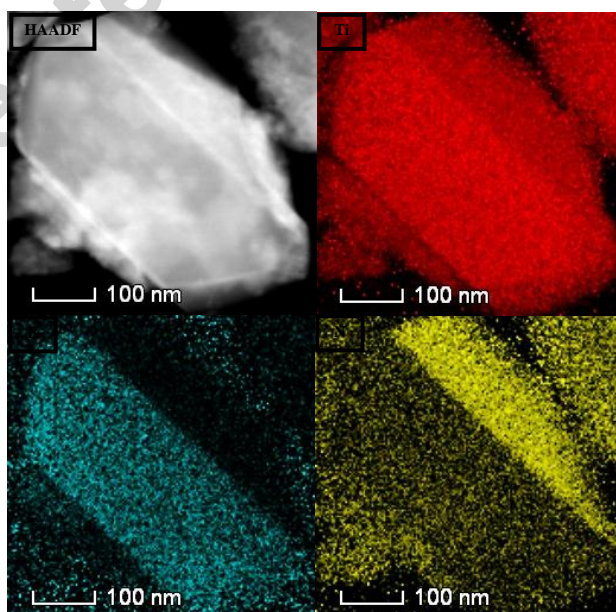


Figure 3

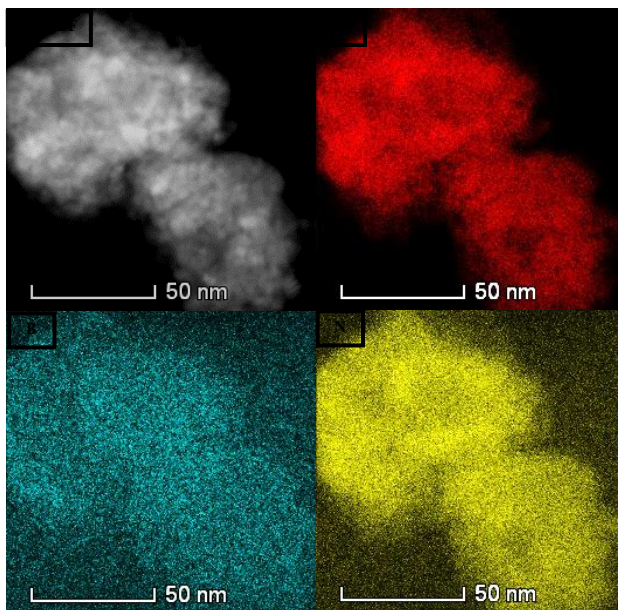


Figure 4

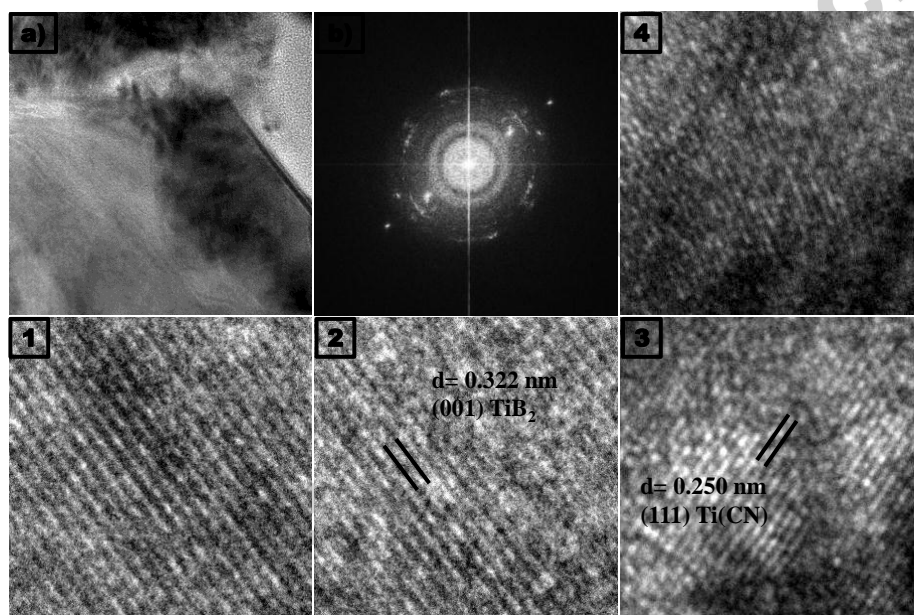


Figure 5

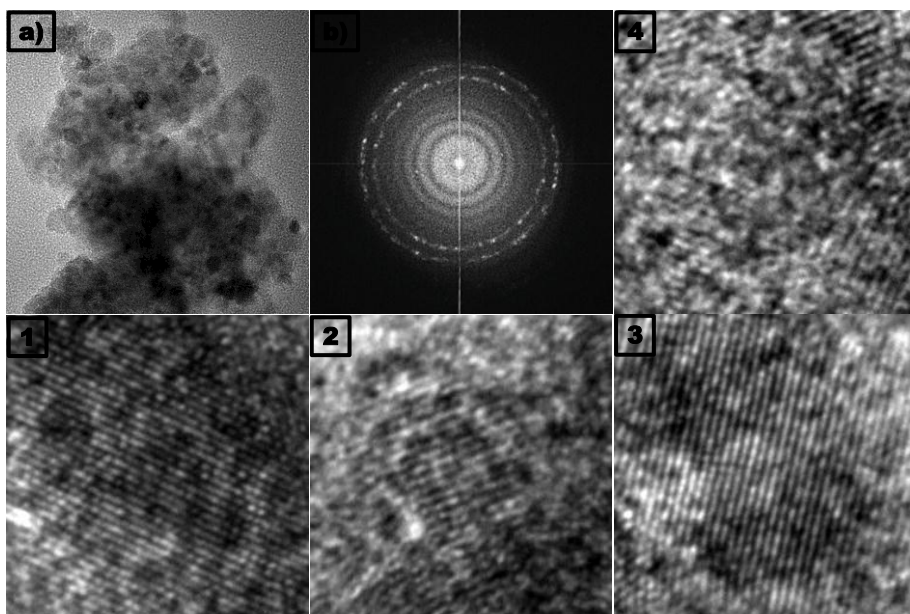


Figure 6

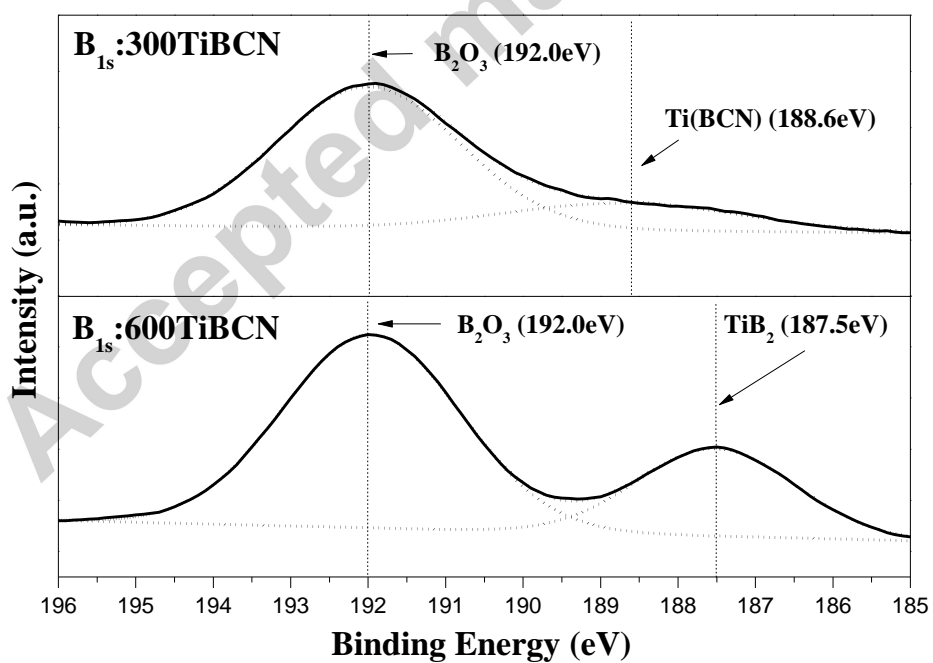


Figure. 7